J. Appl. Comput. Mech., 9(1) (2023) 226-238
DOI: 10.22055/jacm.2022.41006.3689

ISSN: 2383-4536
jacm.scu.ac.ir

Shahid Chamran University of Ahvaz

Journal of Applied and Computational Mechanics

Research Paper

Accuracy and Convergence Rate Comparative Investigation on Polytope Smoothed and Scaled Boundary Finite Element

Boonchai Phungpaingam[1], Suthee Piyaphipat[2], Kamtornkiat Musiket[3]

[1] Department of Civil Engineering, Rajamangala University of Technology Thanyaburi, Pathumthani, 12110, Thailand, Email: boonchai_p@en.rmutt.ac.th
[2] Department of Civil Engineering, Rajamangala University of Technology Thanyaburi, Pathumthani, 12110, Thailand, Email: suthee_p@en.rmutt.ac.th
[3] Department of Civil Engineering, Rajamangala University of Technology Thanyaburi, Pathumthani, 12110, Thailand, Email: kamtornkiat@rmutt.ac.th

Received June 02 2022; Revised August 11 2022; Accepted for publication August 11 2022.
Corresponding author: K. Musiket (kamtornkiat@rmutt.ac.th)

Abstract. Continuity and discontinuity of two-dimensional domains are thoroughly investigated for accuracy and convergence rate using two prominent discretization methods, namely smoothed and scaled boundary finite element. Because of their capability and versatility when compared to primitive elements, N-sided polygonal elements discretized from modified DistMesh and PolyMesher schemes are used. In terms of accuracy and convergence rate, NSFEM and SBFEM are found to be superior to CSFEM and ESFEM regardless of meshing alternative. The best accuracy occurs at NSFEM and SBFEM, and the obtained convergence rates are optimal. Particularly, in the smoothing domain, it is believed that DistMesh has more promising potential than PolyMesher does; yet, in the discontinuity domain, PolyMesher has been discovered to be more powerful while maintaining its efficiency.

Keywords: Polytope, smoothed finite element, scaled boundary finite element, mesh schemes.

1. Introduction

The finite element method (FEM) [1-3] has become a majority used numerical method of development for many decades, and many commercial software packages have been developed based on the FEM theory. An infinitely complex system can be modelled using a finite number of discrete elements in the Galerkin weak formulation. The three-node linear triangular element is the simplest type of finite element in two-dimensional problems, and it can be automatically generated without any manual intervention. When using linear triangular elements, the structural natural frequency will be much higher than the exact value because of their stiffer properties. For dynamic analysis, FEM using linear triangular elements has a low accuracy and low convergence rate [4]. Nonetheless, there are some characteristics of the FEM that it is unable of handling satisfactorily: a) Stress singularities that occur in fracture mechanics problems [5] and b) unbounded domain representation [6]. Additionally, mesh production remains time-consuming and difficult, frequently constituting a significant bottleneck in the analysis pipeline. This issue is particularly acute when considering specialized data formats like as digital pictures and stereolithography (STL), which are now widely embraced by industry.

Numerous alternatives have been presented by researchers to address the aforementioned difficulties, including the smoothed finite element method (SFEM) [7], the boundary element method (BEM) [8], the scaled boundary finite element technique (SBFEM) [9, 10], the extended finite element method (X-FEM) [11], and smoothed extended finite element method [12], to name a few. There has been a great deal of research done in an effort to overcome the FEM's overly stiff property. Standard FEM-based methods, such as hybrid FEM formulations [13, 14], can improve accuracy noticeably, but there are no effective formulations for the triangular/tetrahedral elements that can be automatically generated in complex problems [15]. In two and three spatial dimensions, SFEM models are shaped by the configuration of their own smoothing cells (SCs) or smoothing domains, which commonly contain the cell based, node-based, edge-based, face-based, and αFEM forms [16]. The cell based SFEM (CSFEM) is the earliest and simplest model because it immediately constructs many subcells as smoothing domains within each linear polygonal element. Until date, a various of engineering problem has access to cell based SFEM via some methods for multiplying a quantity and a gradient in the smoothed Galerkin weak form. More accurate results can be obtained by using a smoothing technique [17, 18]. However, in dynamic analysis, NS-excessively FEM's soft stiffness could lead to spurious modes [19].

Alternatively, the SBFEM was first introduced as a semi-analytical method for simulating wave propagation in unbounded domains. As a result of this expansion in recent years, the SBFEM has been used for a wide range of applications, including wave propagation in confined domains [20]. The SBFEM can be considered a universal numerical approach for solving PDEs because of its adaptability and wide range of applications. SBFEM has a number of improvements over regular FEM, the most significant of which is the ability to generate polytope elements with any number of vertices, edges, or surfaces. As a result of this benefit,

Published online: August 22 2022

meshing time in the typical FEM is greatly reduced. Firstly, the SBFEM is extremely complementary to the hierarchical tree-based mesh generation technique, which is a robust mesh generation technology that can automatically discretize difficult geometries with highly irregular boundaries [21]. SBFEM investigations of two- and three-dimensional issues have both used polytope elements in recent years [22]. Computer tomography (CT) scans or STL files, commonly used in 3D printing, can both be utilized to store the geometric data. Second, meshes with rapid transitions in element size are possible with polytope elements [23], which is useful for simulating complicated domains. Small element sizes are required at the border of complicated structures, such as particle reinforced composites, human bones, or other micro-structured materials, in order to create analysis-ready meshes. In order to reduce the number of components and the computational resources necessary, we need transition elements that allow nearby polytope elements to have varying sizes. It is also possible to transform non-matching interface meshes to matching ones by separating interface edges (2D) or surfaces (3D) because of the greater flexibility in polytope elements [24]. Analyses involving many domains benefit from applying interface constraints more easily thanks to the matching discretization at the interface.

In classical FEM, the only topological shapes are triangles and quadrilaterals. A high-quality element is critical to the FEM's computational precision and dependability. High-quality meshes and complex re-meshing procedures are often required to improve computational precision. A frequent solution to large-scale difficulties is to utilize a local fine mesh in the area of interest. Using distorted meshes can invalidate the solution in the areas where coarse and fine meshes meet. It wasn't until the 1970s that appropriate first-order shape functions were available for element geometries with more than four sides Using perspective geometry concepts, Wachspress [25], developed a new form of shape functions called as Wachspress shape functions. For elements with more than four nodes, rational functions are used to obtain linear relations in shape functions that are linear. A look at the shape functions reveals that they are made up of complex rational functions that require specialized methods to solve. It was at the turn of the century that the Wachspress method was reconsidered and garnered additional attention. Polygonal/polyhedral finite components and difficulties within polygonal/polyhedral meshes have been the subject of numerous methods over the years. Recently, adaptive polygonal finite element for cracked limit analysis was developed using universal technique for mesh refining based on the concept of a so-called polytree mesh. This approach works very well for classic triangle and quadrilateral element. In addition, conforming polytree meshes can be thought of as a generalization of quadtree meshes [26].

Among those reputation automatic mesh generation techniques, DistMesh [27] and PolyMesher [28] are very versatile, easy to use, and yet powerful tool for their works. In former, unstructured triangular and tetrahedral meshes can be generated with Signed Distance functions to define the geometries, making it easy to understand. DistMesh employs the Delaunay triangulation technique to generate the mesh and uses a force-based smoothing procedure to find the best node placements. Delaunay makes frequent revisions to the topology. Using the distance function, the boundary points can only move tangentially to the boundary. Meshes produced by this iterative process are often of excellent shape. Polytope element can be constructed via modification of this mesh scheme with ease.

The latter, implicit representation and the discretization of the domain using Centroidal Voronoi diagrams are the primary components. The signed distance function contains all of the information required by mesh algorithm regarding the meshing domain. This implicit description enables the construction of a relatively wide class of domains using algebraic expressions. The domain is discretized using a Centroidal Voronoi Tessellation (CVT) that incorporates an approximation to the domain's boundary. The approximation is achieved by incorporating the set of seeds' reflections combining with Lloyd's approach to ensure that seeds are distributed uniformly, resulting in a high-quality mesh finally [29]. We note that CVTs have previously been used to generate and analyze triangle discretization and that super convergence of numerical solutions has been seen in some circumstances.

The main goal of this paper is to investigate the effect of automatic meshing method for polytope elements used in SFEM and SBFEM. The continuity and discontinuity of domains are considered as numerical benchmark problems. A former is a cantilever Bernoulli-Euler beam, and the latter is a castellated cantilever beam with five circular holes. Plane stress condition is assigned. For each category, both automatic mesh generation will be manipulated with various mesh refinement. Three main SD schemes, namely nCSFEM, nNSFEM, and nESFEM, for smoothed finite element analysis will be statically analyzed comparing with n-sided polytope scaled boundary finite element. Accuracy and convergence rate at various mesh refinement will be scrutinized side-by-side and reported eventually.

The remaining part of this paper is organized as follows: A brief review of the theoretical derivations of the SBFEM is presented in Section 2. Section 3 introduces the fundamentals of the SBFEM and its formalism. The numerical examples include academic benchmark tests meshed by different automatic meshing techniques clearly demonstrating the analysis results in Section 4. Results and important conclusion are provided in Sections 5 and 6, respectively.

2. Smoothed Finite Element Formulations

2.1 Gradient strain smoothing

Consider a solid mechanics problem whose problem domain is initially separated into a set of elements, which are then connected to form a mesh, as in a typical FEM. Because the S-FEM uses smoothed strains, smoothing domains must be added to the element mesh. As a result, the interesting domain is subdivided into a number of non-overlapping and non-gap smoothing zones Ω_k^s bounded by boundary $\Gamma_k^s (k = 1,2,\ldots,Ns)$ where Ns is smoothing sub domains. The smoothed strain can then be calculated for any points within a smoothing domain using the smoothed strain formula.

$$\bar{\varepsilon}_k = \int_{\Omega_k^s} \nabla \mathrm{u}^h(\mathrm{x}) \mathrm{W}_k(\mathrm{x}\text{-}\mathrm{x}_k) d\Omega \tag{1}$$

where term $\nabla \mathrm{u}^h$ denotes a compatible strain field calculated from assumed displacement, as in conventional FEM, and $W_k(\mathrm{x} - \mathrm{x}_k)$ denotes a weight function satisfying both the unity and the positiveness conditions of the weight function. The Heaviside-step function is the simplest and most widely used of these functions, despite its simplicity. Applying those ingredients into Eq. (1) and, using divergence theorem, we are able to obtain the smoothed strain field as follows:

$$\bar{\varepsilon}_k = \frac{1}{\mathrm{V}_k^s} \int_{\Omega_k^s} \nabla \mathrm{u}^h(\mathrm{x}) d\Omega = \frac{1}{\mathrm{V}_k^s} \int_{\Gamma_k^s} \mathrm{L}_n(\mathrm{x}) \mathrm{u}^h(\mathrm{x}) d\Gamma \tag{2}$$

where V_k^s means volume of smoothing domain (area for 2D), $\bar{\varepsilon}_k$ is the compatible strain obtained by differentiation from the assumed displacements, and $\mathrm{L}_n(\mathrm{x})$ represents unit normal outward matrix of each smoothing cell boundary Γ_k^s. It is worth noting that the smoothed strain field in Eq. (2) will be computed using a boundary integration method rather than a domain integration method.

Following the establishment of a smoothed strain field, it is simple to compute a smoothed strain-displacement matrix $\bar{B}$ in 2D using the smoothed strain-displacement matrix B formula.

$$\bar{\varepsilon}(x) = \sum \bar{B}_k \bar{d}_k \tag{3}$$

where

$$\bar{B}_k = \frac{1}{A_k^s}\int_{\Gamma_k^s} n^s(x) N_I(x) d\Gamma = \begin{bmatrix} \bar{b}_{kx} & 0 & \bar{b}_{ky} \\ 0 & \bar{b}_{ky} & \bar{b}_{kx} \end{bmatrix} \tag{4}$$

where A_k^s is area of smoothing domain.

When only one numerical integration Gauss rule provides sufficient solution accuracy and is calculated along each boundary edge of smoothing cells, the last term in Eq. (4) can be alternately replaced by algebraic summation form as shown in the following

$$\bar{b}_{kx}(x) = \sum_{k=1}^{n_\Gamma^s} N_I(x_k^{gp}) L_k n_{m,k}, \; m = x, y \tag{5}$$

n_Γ^s represents the number of polygonal sides, x_k^{gp} represents the Gauss point located in the middle of the corresponding edge according to outward unit normal vector, $n_{m,k}$, and L_k represent the length of the corresponding edge, according to outward unit normal vector. As can be seen in Eqs. (4) and (5), there is no need to take the derivative of shape function because it is already defined. Finally, the smoothed global stiffness matrix $\bar{K}$ building process is absolutely relevant to the standard FEM scheme with interchangeable terminology for elements and smoothing cells. The computation and creation of the smoothed stiffness matrix K are quite similar to the processes used in the classic finite element method (FEM). Using the sub-stiffness-matrices from all of the smoothing domains, it is possible to construct a complete stiffness matrix.

$$\bar{K}_{ij} = \sum_{k=1}^{N_s} \bar{B}_{ik}^T E \bar{B}_{jk} V_k^s \tag{6}$$

A similar method to that used in the FEM is employed to derive the equation shown above. Essentially, the difference is that FEM is element based, whereas S-FEM is structure based. Existing FEM assembly techniques can be utilized for S-FEM by simply considering the smoothing domains as "elements," in the same way that they are treated in the FEM.

2.2 Smoothing domain classification for 2D

The art of the SFEM is in devising novel techniques to generate various types of smoothing domains, which results in a variety of SFEM models. It first begins by generating smoothing domains from the elements contained in a domain mesh. For instance, in the CSFEM, quadrilateral elements with four nodes (Q4) may be used. In this scenario, as illustrated in Fig. 1, one Q4 element can be separated into desired smoothing domains. Each smoothing domain is quadrilateral in shape and is bounded by four boundary segments. They are all supported by the same Q4 element with four nodes. Figure 1 shows the smoothing cells/domains created by the CSFEM, the earliest S-FEM model. As with FEM, the bandwidth of the stiffness matrix in CSFEM is identical to that in FEM's numerical implementation. Some commercial finite element software programs, such ABAQUS® [30] user-defined elements, allow the CSFEM to be implemented using user-defined subroutines because the smoothing operations are handled within the elements themselves, rather than by manipulating elements across boundaries.

Additionally, it is feasible to employ four SDs for some elements and one SD for others in the mesh, but this idea has not been implemented or thoroughly researched thus far.

When n-sided polygonal components are utilized, it is possible to generate smoothing domains based on edges, resulting in ESFEM-Polytope models for 2D issues, as illustrated in Fig. 2 Each edge has its own smoothing domain in this example, and the total number of smoothing domains equals the number of edges in the mesh. A smoothing domain for an edge that is included inside the issue domain; the edge-based smoothing domain is a four-sided polygon with two supporting elements and four-line segments defining the smoothing domain boundary. An inner edge-based smoothing domain has four supporting nodes. For an edge on the problem domain boundary that is a triangle and has just three-line segments on the smoothing domain border. For a boundary edge-based smoothing domain, the number of supporting elements is one and the number of supporting nodes is three. On the basis of edge-based smoothing domains that are generated associated with edges of T-elements, ESFEM analyzes the weak form. There has been an emphasis on T-elements in ESFEM development thus far because of the advantages they provide in terms of automated mesh production and adaptive mesh rezoning.

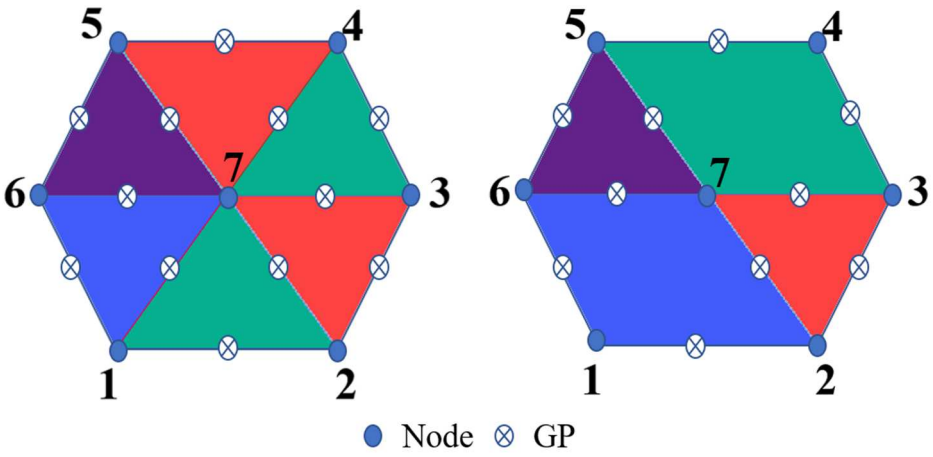

Fig. 1. Smoothing cells forming.

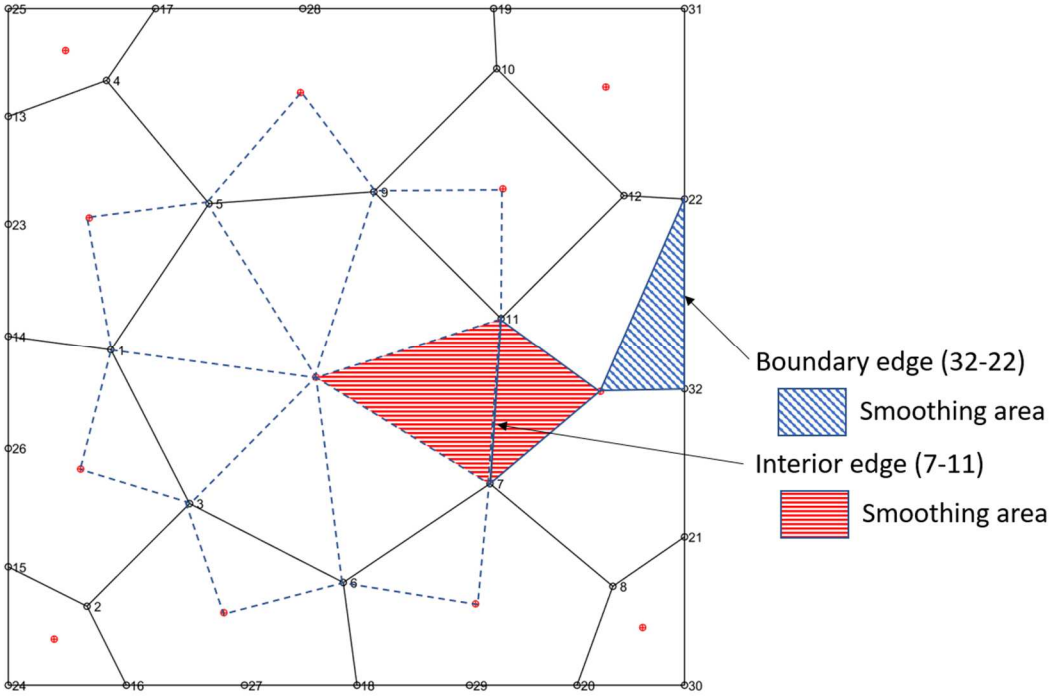

Fig. 2. ESFEM smoothing cell establishment.

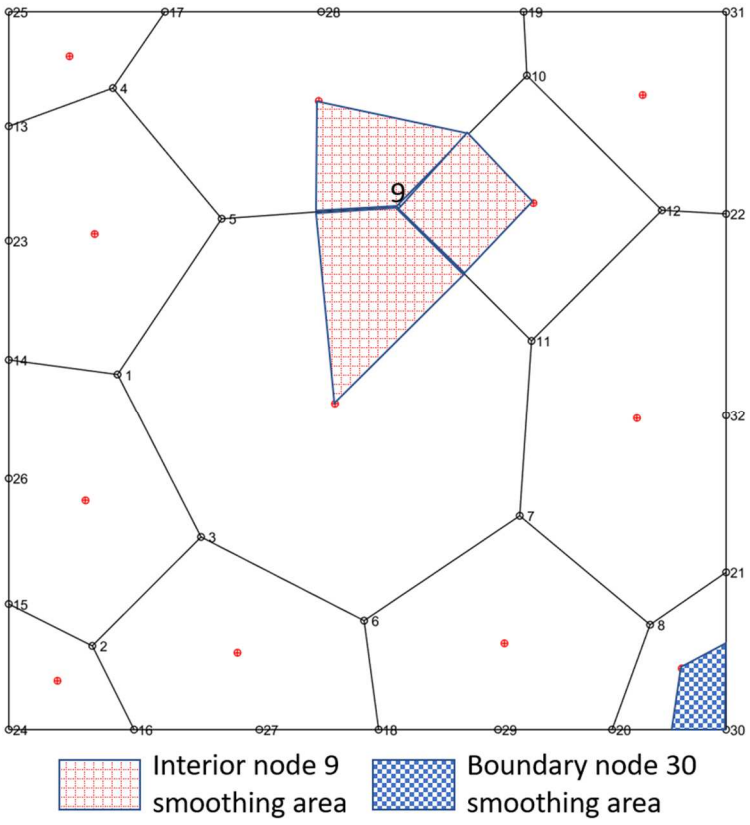

Fig. 3. NSFEM smoothing cells creation.

As illustrated in Fig. 3, an NSFEM model makes use of node-based smoothing domains, which are built based on nodes to smooth out the kinks. A smoothing domain is a polygon surrounded by numerous line segments that is formed via smoothing. Any segment connects the midpoint of an edge to the center of a polygonal element that is connected to the node, regardless of the type. An isolated node on the problem boundary might result in a one-sided node-based smoothing domain, and the number of supporting nodes is typically smaller. In principle, as illustrated in Fig. 3, a node-based smoothing domain can include contributions from any number of elements inside it. The linear conforming point interpolation method (LC-PIM) [31] and, when the RBFs are incorporated subsequently, the linearly conforming radial point interpolation method (LC-RPIM) [32] were the first inspirations for the NSFEM. In this method, the strain smoothing is carried out over the smoothing domain that encompasses the nodes in the model.

3. Fundamental Scaled Boundary Finite Element

It was first created for the dynamic analysis of unbounded domains where radiation boundary conditions are defined at infinity, and it has since been extended to other applications [33]. The division of a problem domain into subdomains allows for the fulfillment of scaling requirement. Subdomains, on average, have more intricate shapes than finite elements. The scaled boundary finite element method is a semi-analytical method that is used to generate an estimated solution for a boundary problem. The bounds of the entire subdomain, on the other hand, are just discretized. Analytical procedures are employed in order to discover the solution when looking in the opposite direction. As opposed to the typical finite element technique, there is no requirement to make an a priori choice of interpolation functions over the subdomain/element. Due to the use of an adjacent cell of finite elements for mechanically based derivation, this method was originally known as the "consistent infinitesimal finite-element method." However, this method has since been renamed the "consistent finite-element method" due to the use of an adjacent cell of finite elements. With the help of the Galerkin weighted residual technique, [9] were able to develop the scaled boundary finite element method, which they dubbed the 'scaled boundary finite element method' in their paper. Deeks and Wolf describe a virtual work-based derivation that is based on virtual work [34].

3.1 Geometry transformation

Any arbitrary polygon can be considered as a sub-domain in the scaled boundary finite element method, as illustrated in Fig. 4. In the polygon, a so-called scaling center, denoted by the letter 'O,' is chosen. The geometry of the polygon must only meet the scaling criterion, which means that the entire boundary must be visible when viewed from the center of the scaling. This group of polygons includes regular polygons as well as a large number of irregular and convex polygons. The portion of the border that is directly visible from the scaling center is discretized into isoparametric line elements, which can be created in any arbitrary order by connecting adjacent elements. The nodal coordinates at the extremities of each line element are organized in the direction of x and y axis rotation. To characterize the sub-domain, the border is scaled with the dimensionless radial coordinate, starting at the scaling center 'O', where ξ equals zero, and ending at the boundary, where ξ equals one. In this study, we will only consider two-dimensional bounded elements, i.e., ξ are a number between 0 and 1. When a line element is on the boundary, its geometry is given by its nodal coordinates and the one-dimensional shape functions defined on the local coordinate $-1 \le \eta \le 1$ (Fig. 5).

SBFEM elements are integrated analytically along the radial direction and approximated by polynomials in the circumferential direction, as opposed to FEM elements, which are integrated analytically along the radial direction and approximated by Gaussian quadrature. As shown in Fig. 2(a), the SBFEM model for an arbitrary n-sided polygon element can be used to simulate a variety of shapes. Because the polygon's geometry must adhere to a scaling requirement, it is necessary to choose a scaling center that is visible from every point on the boundary. Figure. 5(b) shows how the boundary of a polygon is discretized using line elements with shape function and natural coordinates in a counterclockwise manner.

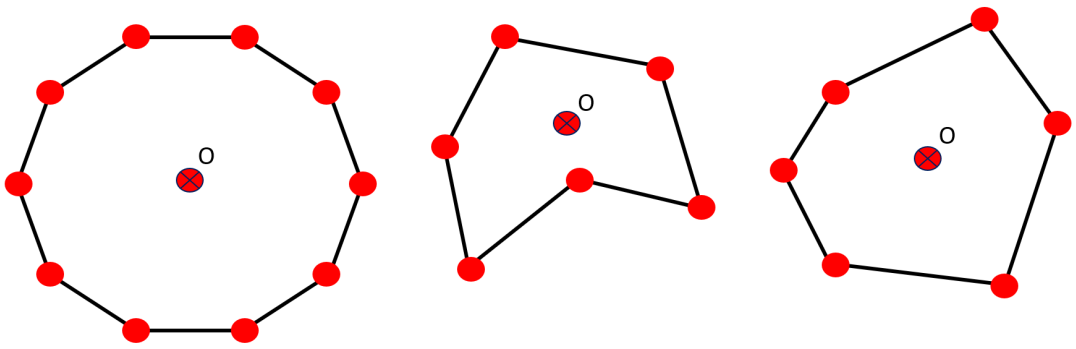

Fig. 4. N-Sided Polytope elements.

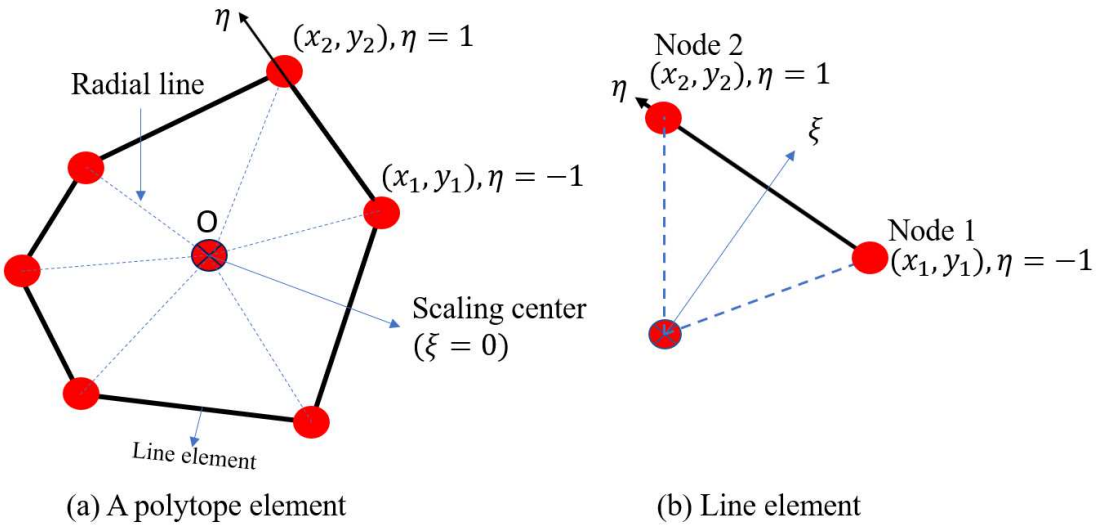

Fig. 5. Scaling boundary edge.

3.2 Displacement, strain, and stress field

The following is the expression for the geometry of the element described by the coordinates on the boundary:

$$X_b(\eta) = N(\eta)X_b \tag{7}$$

where, X_b denotes the nodal coordinate vectors of line element, and $N(\eta)$ denotes the one-dimensional shape function corresponding to the nodal coordinate vectors. In order to obtain the surface of the element, the discretized boundary must be scaled in the direction of the scaling center along the radial direction. A new radial coordinate, denoted by the symbol ξ, is introduced, with $\xi = 0$ at the scaling center and 1 at the boundary. When considering a triangular sector, the displacement field $u(\xi,\eta)$ at any point can be expressed as

$$u(\xi,\eta) = N_u(\eta)u(\eta) \tag{8}$$

where u corresponds to radial displacement functions along a line connecting the scaling center and a node at the boundary. The strain field in scaled boundary coordinates is expressed as

$$\varepsilon(\xi,\eta) = B_1(\eta)u(\xi)_{,\xi} + \xi^{-1}B_2(\eta)u(\xi) \tag{9}$$

The Hooke's law is used to connect stresses to strains at any point in the subdomain using the elasticity constitutive matrix D as

$$\sigma(\xi,\eta) = DB_1(\eta)u(\xi)_{,\xi} + \xi^{-1}DB_2(\eta)u(\xi) \tag{10}$$

where

$$B_1(\eta) = \frac{1}{|J(\eta)|}\begin{bmatrix} y(\eta)_{,\eta} & 0 \\ 0 & -x(\eta)_{,\eta} \\ -x(\eta)_{,\eta} & y(\eta)_{,\eta} \end{bmatrix}, B_2(\eta) = \frac{1}{|J(\eta)|}\begin{bmatrix} -y(\eta)_{,\eta} & 0 \\ 0 & x(\eta)_{,\eta} \\ x(\eta)_{,\eta} & -y(\eta)_{,\eta} \end{bmatrix} \tag{11}$$

and $|J(\eta)|$ is determinant of the Jacobian matrix for coordinate transformation.

3.3 Governing equations in scaled boundary finite element

It is possible to apply Galerkin's weighted residual approach [9] or the virtual work method [34] in the circumferential direction to get the scaled boundary finite element equation in displacement, which may be represented as:

$$E_0\xi^2 u(\xi)_{,\xi\xi} + (E_0 - E_1 + E_1^T)\xi u(\xi)_{,\xi} - E_2 u(\xi) = 0 \tag{12}$$

where $u(\xi)_{,\xi\xi}$ and $u(\xi)_{,\xi}$ are the first and second order derivatives, respectively, of u with respect to ξ. $E_i (i = 0,1,2)$ are the coefficient matrices defined in Eqs. (13)-(15):

$$E_0 = \int_{-1}^{1} B_1^T(\eta)DB_1(\eta)|J(\eta)|d\eta \tag{13}$$

$$E_1 = \int_{-1}^{1} B_2^T(\eta)DB_1(\eta)|J(\eta)|d\eta \tag{14}$$

$$E_2 = \int_{-1}^{1} B_2^T(\eta)DB_2(\eta)|J(\eta)|d\eta \tag{15}$$

The second order differential equation in Eq. (12) can be changed by first translating it into a first order ordinary differential equation with twice as many unknowns as the second order differential equation

$$\xi\begin{bmatrix} u(\xi) \\ q(\xi) \end{bmatrix} = -Z\begin{bmatrix} u(\xi) \\ q(\xi) \end{bmatrix} \tag{16}$$

where Z is a Hamiltonian matrix

$$Z = \begin{bmatrix} E_0^{-1}E_1^T & -E_0^{-1} \\ E_1E_0^{-1}E_1^T - E_2 & -E_1E_0^{-1} \end{bmatrix} \tag{17}$$

and $q(\xi)$ is the internal nodal force vector along radial line

$$q(\xi) = E_0\xi u(\xi)_{,\xi} + E_1^T u(\xi) \tag{18}$$

Following the work of Song [35], a block diagonal Schur decomposition of Z in Eq. (16) is then performed, resulting in

$$Z = \begin{bmatrix} \Psi_{u_n} & \Psi_{u_p} \\ \Psi_{q_n} & \Psi_{q_p} \end{bmatrix} = \begin{bmatrix} \Psi_{u_n} & \Psi_{u_p} \\ \Psi_{q_n} & \Psi_{q_p} \end{bmatrix} \begin{bmatrix} S_n & \\ & S_p \end{bmatrix} \tag{19}$$

S_n and S_p are upper triangular matrices with diagonal eigenvalues that contain negative and positive real components, respectively. Only the eigenvalues with negative real portions are evaluated for confined domains, resulting in finite displacements at the scaling center. Transformation matrices that correspond to displacements or internal forces are represented by the variable. The stiffness matrix for a linear elastic element is obtained using the solution of Eq. (16).

$$K_e = \Psi_{q_n} \Psi_{u_n}^{-1} \tag{20}$$

The strain field epsilon can be expressed as

$$\varepsilon = B(\xi, \eta) u_b \tag{21}$$

where u_b is the node displacement and $B(\xi, \eta)$ is the scaled boundary strain–displacement matrix:

$$B(\xi, \eta) = \Psi_{\varepsilon}(\eta) \xi^{-S_n - I} \Psi_{u_n}^{-1} \tag{22}$$

with $\Psi_{\epsilon}(\eta)$ as the mode of strain. Eventually, the SBFEM yields a global system of algebraic equations identical to FEM, denoted as

$$Ku=F \tag{23}$$

where the stiffness matrix $\mathbf{K}$ and the load vector $\mathbf{F}$ are assembled using the same method as FEM.

4. Benchmark Problems

Two groups of benchmark problems representing smoothing and non-smoothing problem domain in each group is assigned. The former is a classical Bernoulli-Euler beam representing continuity domain with length $L = 48$ and height $h = 12$. Homogeneous essential boundary condition is employed on one ended while bending moment $M = 100$ is applied at free ended. Material properties are $E = 10^7\ kPa$ and Poisson's ratio $\nu = 0.28$ with plane stress conditions were noticed in this analysis. The latter is a castellated beam representing discontinuity problem domain by introducing five circular holes cut from an ordinary beam. All beam's dimensions are chosen identically to previous model for consistency. Elastic modulus and Poisson's ration are equal to $E = 10^7\ kPa$ and $\nu = 0.28$, respectively. The free ended is subjected to downward shear traction 1,000. Dirichlet boundary conditions preventing rigid body motions in two dimensional for plane stress analysis are occupied on the left side of the benchmark problems. Figure 6 depicts more details for both numerical models. For consistency, meshing was established in such a way that number of elements are analogous among discretization analysis methods. Mesh refinement is exploited such that numbers of node are analogous for each categories mesh schemes of analysis.

The exact solution of displacements and stresses for beam's continuity domain is given by

$$\begin{aligned} u &= -\frac{M}{EI} xy,\ y = 0.5 \frac{M}{EI} \left(x^2 + \nu \left(y^2 - 0.25 h^2 \right) \right) \\ \sigma_x &= -\frac{M}{EI} y,\ \sigma_y = 0,\ \tau_{xy} = 0 \end{aligned} \tag{24}$$

For discontinuity castellated beam, Fig. 6(b), a commercial finite element software namely ABAQUS® modeled with fine meshes will be referred to the numerical results because the exact solutions (or nearly closed-to-exact solution) are not available. Quadrilateral elements are preferable to triangular ones when it comes to solving a two-dimensional plane stress problem. When the control parameter is number of nodes, Fig. 7(a, b) shown different meshing schemes between Distmesh and PolyMesher for specific continuity domain at coarse meshes while Fig. 7(c, d) demonstrated for castellated beam as well.

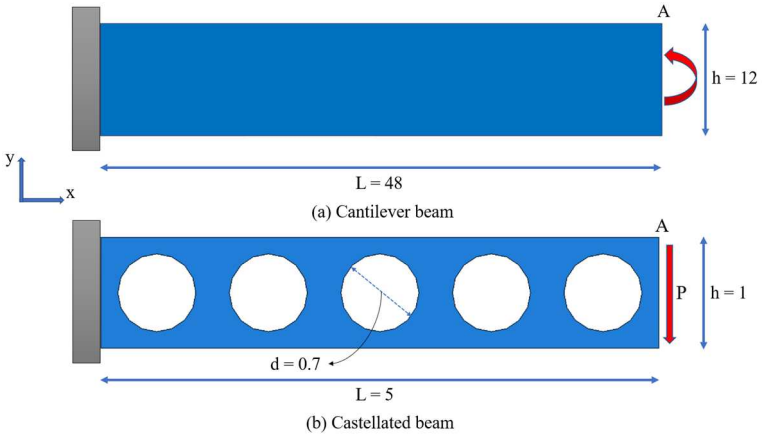

Fig. 6. Continuity and discontinuity beams.

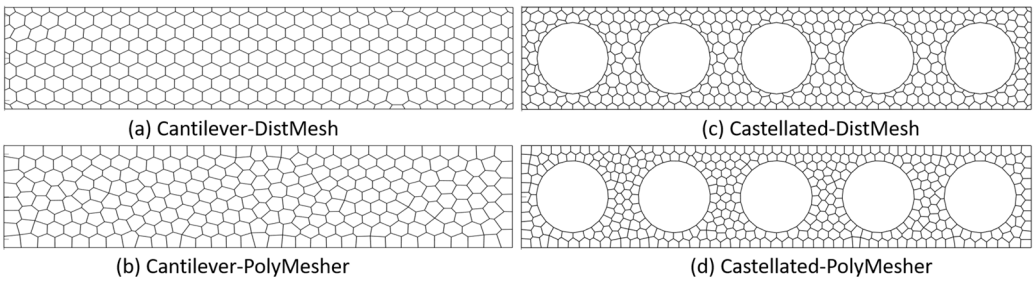

Fig. 7. Modified DistMesh and PolyMesher schemes for beams.

A second group for this simulation is depicted namely an L-Shape panel in Fig. 8(a), and plate with circular hole under remote uniaxial tension, Fig. 8(b), representing continuity and discontinuity analogous to the first group previously. For a former, the dimensions shown here are $b = 1$, $E = 10^7\ kPa$, and $\nu = 0.28$ respectively. On the top edge of panel, a uniformly distributed surface traction $T = 100$ unit is applied. The vertical and horizontal displacement along bottom and right edges are constrained preventing rigid body motions. The latter problem is modeled by substituting the infinite plane with a 2x2 square plate surrounding the circular hole with diameter $a = 0.4$. Elastic modulus and Poisson's ratio are $10^3\ kPa$ and 0.28 respectively. As a boundary condition on the four sides of the square, the exact displacement solution (Eqs. (25, 26)) is specified. Plane stress condition is assumed for both problems. Discretization employed are shown in Fig. 9(a, c) for DistMesh and Fig. 9(b, d) for PolyMesher as intermediate level of mesh refinement.

The analytical stresses solution can express in term of distance from the center of circular hole measured in polar coordinates (r,θ) as

$$\begin{aligned}
\sigma_x &= \frac{T}{2}\left(2-\frac{a^2}{r^2}\left(3\cos 2\theta+\left(2-3\frac{a^2}{r^2}\right)\cos 4\theta\right)\right)\\
\sigma_y &= -\frac{Ta^2}{2r^2}\left(\cos 2\theta-\left(2-3\frac{a^2}{r^2}\right)\cos 4\theta\right)\\
\tau_{xy} &= -\frac{Ta^2}{2r^2}\left(\sin 2\theta+\left(2-3\frac{a^2}{r^2}\right)\sin 4\theta\right)
\end{aligned} \tag{25}$$

and

$$\begin{aligned}
u_x &= \frac{Ta}{8G}\left(\frac{r}{a}(1+\kappa)\cos\theta+\frac{2a}{r}\left((1+\kappa)\cos\theta+\cos 3\theta\right)-2\frac{a^3}{r^3}\cos 3\theta\right)\\
u_y &= \frac{Ta}{8G}\left(\frac{r}{a}(\kappa-3)\sin\theta+\frac{2a}{r}\left((1-\kappa)\sin\theta+\sin 3\theta\right)-2\frac{a^3}{r^3}\sin 3\theta\right)
\end{aligned} \tag{26}$$

for displacement while G and κ are shear modulus and Kolosov constant respectively.

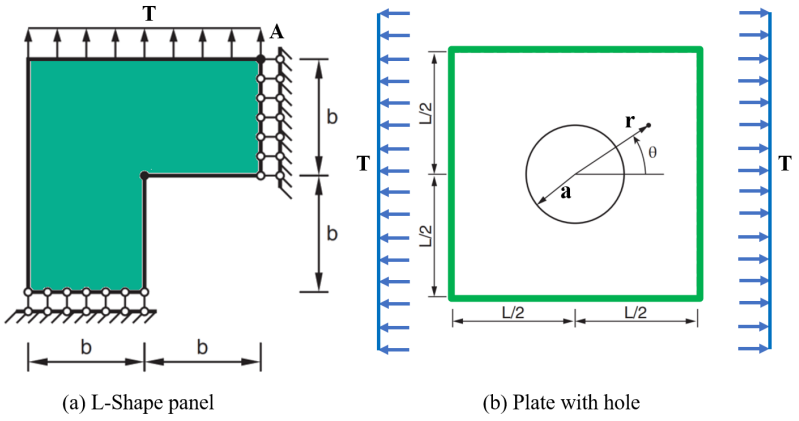

Fig. 8. L-Shape and plate with circular hole.

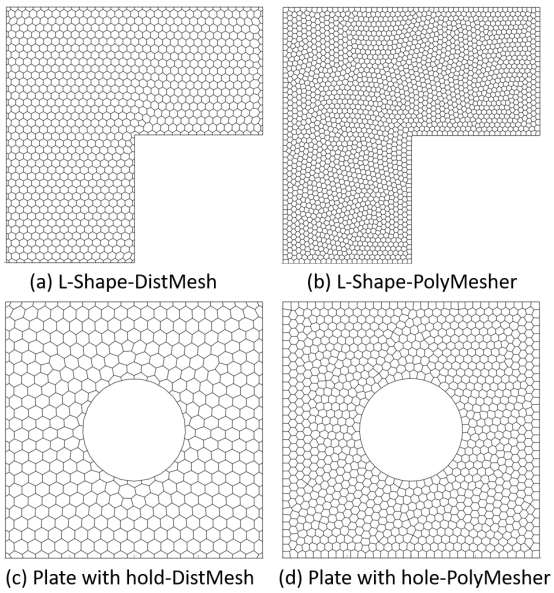

Fig. 9. Modified DistMesh and PolyMesher schemes for L-Shape panel and plate with hold.

$$\kappa = \begin{cases} \dfrac{3-\nu}{1+\nu} & \text{for plane stress} \\ 3-4\nu & \text{for plane strain} \end{cases} \tag{27}$$

Typically, the accuracy of computed results can be measured by relative error in L^2-norm and energy norm and can be calculated by the following equations:

- Relative error in L^2 norm

$$\frac{\left\|\left(u-\Pi u^h\right)\right\|_{L^2}}{\|u\|_{L^2}} = \sqrt{\frac{\sum_{E\in\Omega^h}\int_E \left(u-\Pi u^h\right)^T\left(u-\Pi u^h\right)dE}{\sum_{E\in\Omega^h}\int_E \|u\|^2\,dE}} \tag{28}$$

- Relative error in H^1 energy norm

$$\frac{\left\|\left(u-\Pi u^h\right)\right\|_{\varepsilon}}{\|u\|_{\varepsilon}} = \sqrt{\frac{\sum_{E\in\Omega^h}\int_E \left(\varepsilon(u)-\varepsilon(\Pi u^h)\right)^T C\left(\varepsilon(u)-\varepsilon(\Pi u^h)\right)dE}{\sum_{E\in\Omega^h}\int_E \varepsilon(u)^T C\varepsilon(u)dE}} \tag{29}$$

5. Results

5.1 Cantilever beam

Displacement at point A from n-sided polygonal smoothed and scaled boundary finite element are evaluated for comparison including displacement error norms and number of nodes. The exact solution of vertical displacement at point A (Fig. 6(a)) calculated from Eq. (24) is $8.0E-05$. As expected, results from all discretization analyses are converted to the exact solution as their numbers of node has been increased similar to other discretization techniques.

Corresponding to two meshing schemes mentioned previously, for a former one, the vertical displacements at observation point in ascending are $7.6461E-05, 7.8572E-05, 7.9057E-05$ and $7.9974E-05$ for CSFEM, ESFEM, NSFEM, and SBFEM, respectively. The same analogous of vertical displacements obviously can be seen in case of PolyMesher scheme as well. Among polytope smoothed finite element analyses, NSFEM presented better results than the others considering both schemes. On the other hand, polygonal scaled boundary finite element, the effect of two meshing techniques on accuracy cannot be distinguished. Those accuracies at level of finest mesh presented here are closer to the exact ones than smoothed finite element even more than NSFEM.

In aspect of convergence rate, Fig. 10(a, c), error norm versus number of nodes illustrated all analyses using DistMesh scheme graphically. As can be seen, the optimal rate of convergence for static analysis from both NSFEM and SBFEM are achieved. The similar trend can be observed from PolyMesher scheme as well. It is noteworthy that convergence rates from PolyMesher are lower than the first meshing technique insignificantly. Similar trend can be observed for relative error in energy norm in Fig. 10(b, d). Results from NSFEM and SBFEM in DistMesh pattern are better than optimal yet higher than PolyMesher ones.

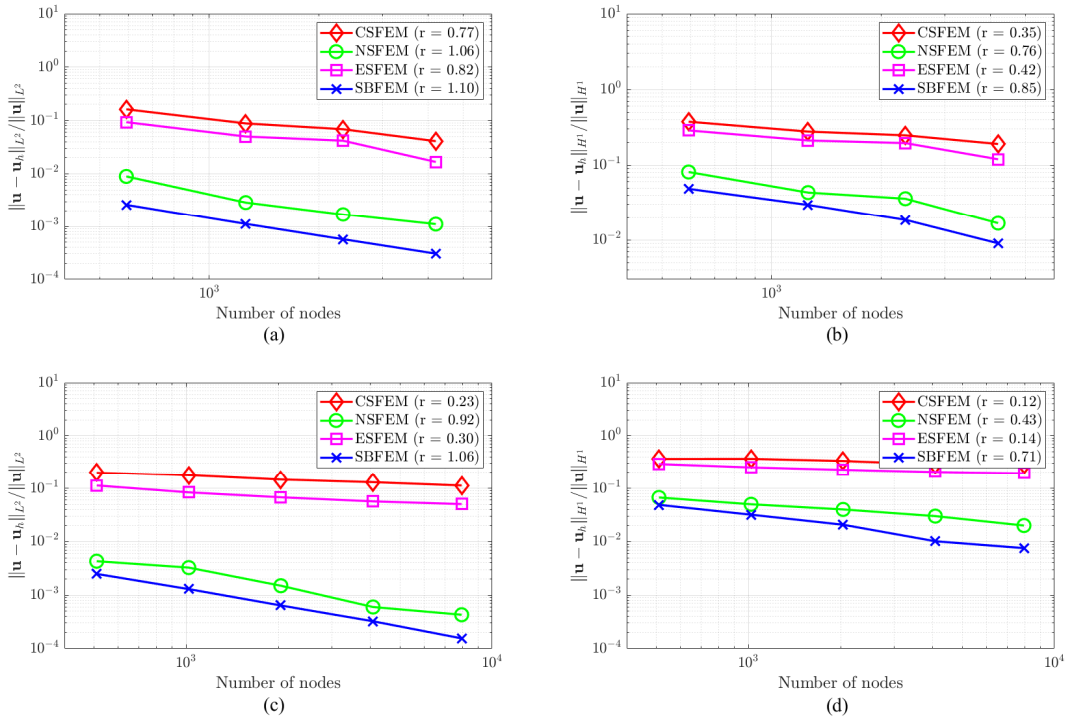

Fig. 10. Relative L^2 norm (a, c) and H^1 seminorm (b, d) as a function of number of nodes for cantilever beam.

5.2 Castellated beam

The reference solution of indicated point A for discontinuity problem domain obtained from fine reduced integration Q4 element in ABAQUS® is -2.73E − 02. The convergence from numerical results to reference one can be obviously achieved as usual mesh refinement. Two groups of results can be distinguished separately. They are plotted against the number of polygonal elements. At finest polytope mesh, the numeral vertical displacements, according to meshing algorithm DistMesh/PolyMesher mentioned previously, are -0.02569/-0.0217, -0.0262/-0.0241, -0.0273/-0.0273, and -0.0272/-0.0272 for CSFEM, ESFEM, NSFEM, and SBFEM, respectively. The most accurate displacement results can be revealed for meshing associated to NSFEM and SBFEM same as continuity domain formerly. NSFEM's solutions had slightly higher accuracy than SBFEM's at lower levels of meshing, but this difference was negligible once the mesh was refined. Both approaches were regarded as having the same level of accuracy for the latter, as can be seen in Fig. 11(a, c). It is noteworthy that the L^2 norm convergence rate of mesh patterns can be split into two distinct categories. NSFEM and SBFEM came up with the most efficient rates, 1.21/1.11 and 0.94/1.11 for DistMesh and PolyMesher, respectively. The SBFEM method was successful in achieving the higher rates of convergence when taking into consideration both meshing patterns. SBFEM with DistMesh scheme produced the consistency convergence rate (1.11), while NSFEM with DistMesh delivered the average precise findings considering the same number of nodes compared to the other analyses.

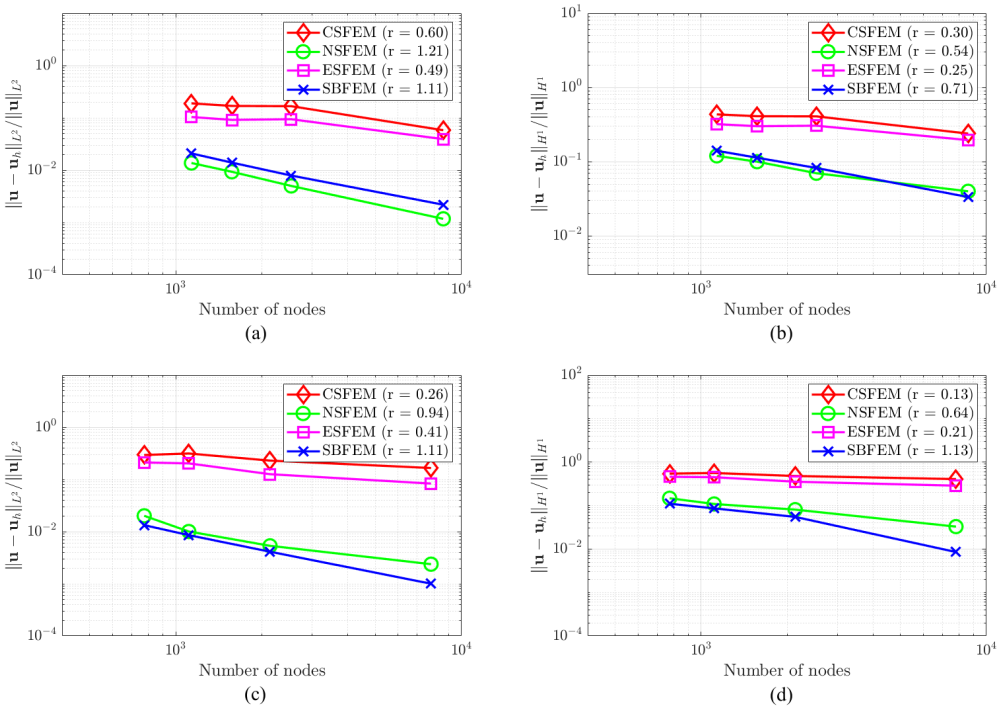

Fig. 11. Relative L^2 norm (a, c) and H^1 seminorm (b, d) as a function of number of nodes for castellated beam.

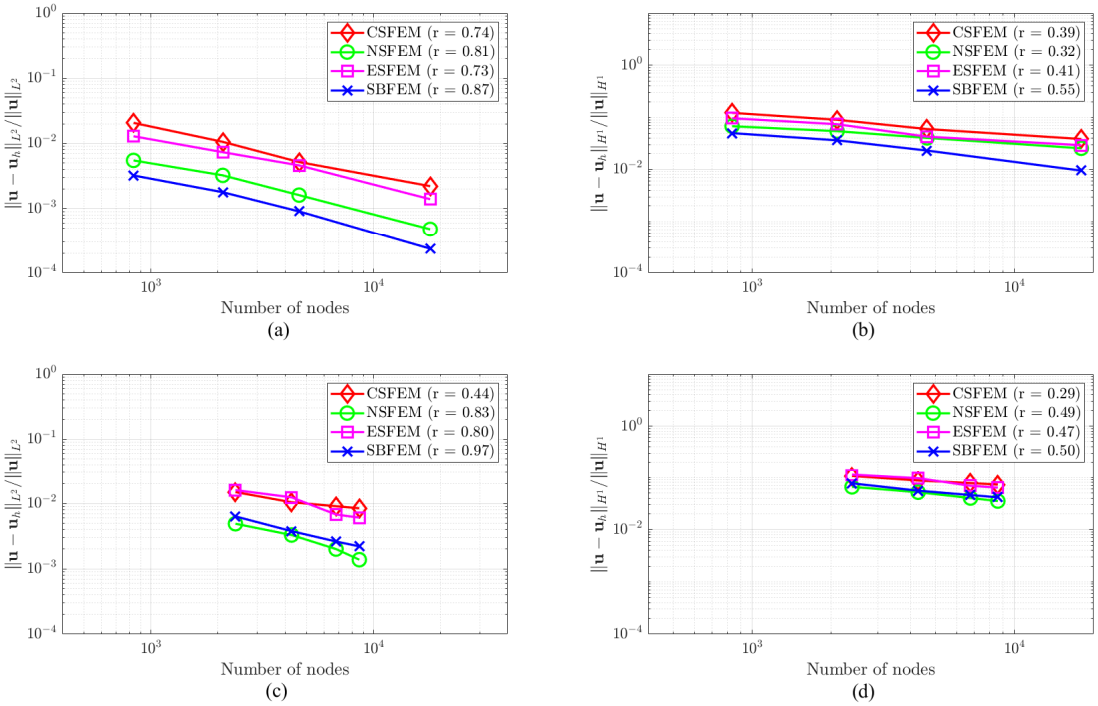

Fig. 12. Relative L^2 norm (a, c) and H^1 seminorm (b, d) as a function of number of nodes for an L-Shape panel.

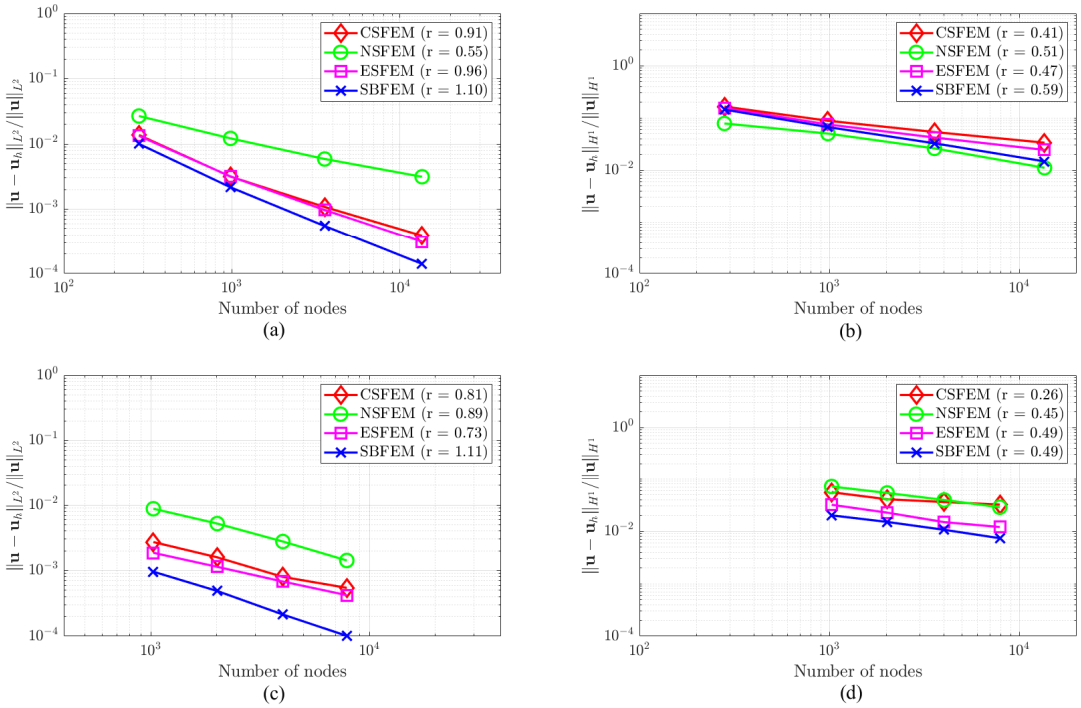

Fig. 13. Relative L^2 norm (a, c) and H^1 seminorm (b, d) as a function of number of nodes for plate with hole.

As for H^1 energy norm, performance of convergence rate from NSFEM and SBFEM passed the optimal rate for both meshing techniques. The highest rate at 1.13 (Fig. 11(d)) has been found when applies PolyMesher scheme to SBFEM as its better geometry representative around the circular hole when mesh refinement. The competitor, NSFEM, has higher values than the optimal rate for H^1 seminorm for both discretization techniques.

5.3 L-Shape panel

Point A at the upper right corner of an L-Shape panel was selected as reference point. A close-to-exact vertical displacement solution obtained from fine mesh simulation using commercial finite element software converged up to 5 digits is 1.0560×10^{-4} and used to evaluate the L^2 error norm. Due to lack of the analytical solution of the vertical displacements at marked point A for evaluating H^1 semi norm or energy norm, *a posteriori error estimation* will be adopted here instead of Eq. (29) for this purpose. The convergence results, with discretization composed of 376, 982, 2208, 8762 and 1200, 2150, 3410, 4340 polygons for DistMesh and PolyMesher, are summarized in Fig. 12. The relative error in the L^2 norm according to Eq. (28) is displayed in Figs. 12(a, c) as a function of the total number of nodes. Figure. 12(b, d) display results that are comparable to those discussed above for the relative inaccuracy in the energy norm (Eq. (29)).

The L^2 norm for all analyses considering both meshing techniques converged at sub-optimal rates. The highest rate for each mesh scheme occurred with SBFEM simulation as 0.87 and 0.97 respectively. This is because of the existing of the stress singularity at its re-entrance corner. Contradictory, SBFEM can keep the optimal rate for H^1 seminorm regardless of mesh algorithms similar to previous examples.

5.4 Plate with hole under remote uniaxial tension

Point A at the upper right corner of a plate was selected as reference point. The exact displacements solution can be calculated directly from Eq. (26) and used to evaluate the L^2 error norm (Eq. (28)). In this illustration, we considered a classic problem involving an infinite plate that has a circular hole with a radius of a = 0.4. This particular problem is depicted in Fig. 8b. A uniaxial tension of the magnitude 1 kPa is applied horizontally to the plate when it is in an infinite state. This analysis is performed using polygonal mesh with 113, 435, 1674, 6556 and 520, 2013, 4018, 7882 polygons for DistMesh and PolyMesher schemes respectively.

The SBFEM is not only the most accurate analysis method in this study but optimal highest L^2 norm convergence rate as well followed by ESFEM which reached the sub-optimal rate as 0.96 and 0.73 for DistMesh and PolyMesher respectively (Fig. 13(a, c)). It is worth mentioned that for PolyMesher scheme, there is a slightly higher L^2 norm for SBFEM compared to DistMesh. In case of H^1 seminorm, except the CSFEM, all analyses maintain the optimal rates according to both mesh schemes as obviously depicted in Fig. 13(b, d).

6. Conclusion

Two discretization approaches, namely smoothed finite element and scaled boundary finite element, were used to examine displacement-based discretization on weak-formulation in depth. As a result of the adaptability of polytope elements, two distinct polygonal meshing approaches, modified DistMesh and PolyMesher, were chosen. Two groups of benchmark problems were numerically simulated, the cantilever beam representing the continuity domain and the castellated beam representing the discontinuity domain in a former while an L-Shape panel and a plate with circular hole under remote tension representing smooth and non-smooth domains, respectively, in the latter. The precision and convergence rate including both L^2 norm and H^1 seminorm on four sets of mesh refinement were evaluated.

Meshing algorithm will influence the accuracy comparison between smoothed and scaled boundary finite elements. The modified DistMesh algorithm for polygonal meshing produced insignificant accurate results than PolyMesher for smoothing domain. This involved that DistMesh has more regularity of edge's length distribution over entire domain than PolyMesher in which at least one edge side is shorter than the others. NSFEM and SBFEM were found to be superior to CSFEM and ESFEM in terms of

accuracy and convergence rate regardless of meshing technique. The differences in overall performance between those methods are insignificant but SBFEM has shown fewer meshing techniques insensitivity than ESFEM. It is noteworthy that even stress singularity exists within problem domain as in an L-Shape panel, the scattered polygonal element from PolyMesher scheme will not affect L^2 norm convergence rate compared to evenly distribution polygonal element in DistMesh.

For non-smoothing domain in castellated beam and a plate with hole, NSFEM and SBFEM still shown the most efficiency way on displacement-based discretization methods over CSFEM and ESFEM without considering of meshing scheme. In aspect of meshing technique for this kind of domain, PolyMesher has displayed superior accuracy compared to DistMesh pattern. As a result of richer representations of the geometry around circular holes, meshes generated by PolyMesher lead to higher accuracy than the mesh created from modified DistMesh. Specifically, a comparison between NSFEM and SBFEM has shown a minor difference in outcomes. Along the circumferential direction of scaled elements in SBFEM which is semi-analytical, its numerical results have demonstrated superior performance, making it one-of-a-kind method appropriate not only for smoothing or non-smoothing domain but insensitive for meshing approach as well.

Author Contributions

B. Phungpaingam and S. Piyaphipat reviewed the analyses and meshing algorithms. K. Musiket dedicated numeral simulation results. The manuscript was written through the contribution of all authors. All authors discussed the results, reviewed, and approved the final version of the manuscript.

Acknowledgements

Authors greatly acknowledge Rajamangala University of Technology Thanyaburi and University of Colorado at Boulder for resources support.

Conflict of Interest

The authors declared no potential conflicts of interest concerning the research, authorship, and publication of this article.

Funding

Not applicable.

Data Availability Statements

The datasets generated and/or analyzed during the current study are available from the corresponding author on reasonable request.

Nomenclature

A_k^s	The area of smoothing domain	r	Distance from the center of circular hole
$\mathbf{a}$	Radial of circular hole	S_n	Upper triangular matrix
$\bar{B}$	Strain-displacement matrix for SFEM	T	Traction
B_1, B_2	Strain-displacement matrix for SBFEM	u	Displacement vector
C, D, E	Elasticity constitutive matrix	V_k^s	Volume of smoothing domain
$\overline{d}_k$	Displacement vector for SFEM	W_k	Weight function
E_0, E_1, E_2	Coefficient matrices for SBFEM	x_k^{gp}	Gauss's point location
G	Shear modulus	Z	Hamiltonian matrix
I	Moment of inertia	Γ_k^s	Boundary of non-overlapping smoothing domain
J	Jacobian matrix	$\overline{\boldsymbol{\varepsilon}}_k$	Smooth strain
K	Stiffness matrix	η, ξ	Circumferential and radial coordinates for SBFEM
L_n	Unit normal outward matrix for smoothing domain	θ	The angle measured from positive x axis
L_k	Length of edges on smoothing domain	κ	Kolosov constant
N_I	Shape function	ν	Poisson's ratio
$n_{m,k}$	Unit normal vector for SFEM	$\sigma_x, \sigma_y, \tau_{xy}$	Stresses
n_Γ^s	Number of polygonal sides	$\Psi_\epsilon(\eta)$	Strain mode
q	Nodal force vector along radial direction		

References

[1] Bathe, K.J., *Finite element method*, Wiley encyclopedia of computer science and engineering, 2007.
[2] Zienkiewicz, O.C., Taylor, R.L., Zhu, J.Z., *The finite element method: its basis and fundamentals*, Elsevier, 2005.
[3] Hughes, T.J., *The finite element method: linear static and dynamic finite element analysis*, Courier Corporation, 2012.
[4] Liu, G., Zhang, G., A normed G space and weakened weak (W2) formulation of a cell-based smoothed point interpolation method, *International Journal of Computational Methods*, 6(1), 2009, 147-179.
[5] Fawkes, A., Owen, D., Luxmoore, A., An assessment of crack tip singularity models for use with isoparametric elements, *Engineering Fracture Mechanics*, 11(1), 1979, 143-159.
[6] Medina, F., Taylor, R.L., Finite element techniques for problems of unbounded domains, *International Journal for Numerical Methods in Engineering*, 19(8), 1983, 1209-1226.
[7] Liu, G.-R., Trung, N., *Smoothed finite element methods*, CRC press, 2006.
[8] Banerjee, P.K., Butterfield, R., *Boundary element methods in engineering science*, McGraw-Hill (UK), 1981.
[9] Song, C., Wolf, J.P., The scaled boundary finite-element method—alias consistent infinitesimal finite-element cell method—for elastodynamics, *Computer Methods in Applied Mechanics and Engineering*, 147(3-4), 1997, 329-355.
[10] Wolf, J.P., *The scaled boundary finite element method*, John Wiley & Sons, 2003.
[11] Belytschko, T., Black, T., Elastic crack growth in finite elements with minimal remeshing, *International Journal for Numerical Methods in Engineering*,

45(5), 1999, 601-620.
[12] Surendran, M., et al., Linear smoothed extended finite element method for fatigue crack growth simulations, *Engineering Fracture Mechanics*, 206, 2019, 551-564.
[13] De Almeida, J.M., De Freitas, J.T., Alternative approach to the formulation of hybrid equilibrium finite elements, *Computers & Structures*, 40(4), 1991, 1043-1047.
[14] Pian, T.H., Wu, C.-C., *Hybrid and incompatible finite element methods*, CRC press, 2005.
[15] Zeng, W., Liu, G., Smoothed finite element methods (S-FEM): an overview and recent developments, *Archives of Computational Methods in Engineering*, 25(2), 2018, 397-435.
[16] Liu, G.-R., The smoothed finite element method (S-FEM): A framework for the design of numerical models for desired solutions, *Frontiers of Structural and Civil Engineering*, 13(2), 2019, 456-477.
[17] He, Z., et al., An improved modal analysis for three-dimensional problems using face-based smoothed finite element method, *Acta Mechanica Solida Sinica*, 26(2), 2013, 140-150.
[18] Li, E., et al., Smoothed finite element method for analysis of multi-layered systems–Applications in biomaterials, *Computers & Structures*, 168, 2016, 16-29.
[19] Nguyen-Thoi, T., et al., A node-based smoothed finite element method (NS-FEM) for upper bound solution to visco-elastoplastic analyses of solids using triangular and tetrahedral meshes, *Computer Methods in Applied Mechanics and Engineering*, 199(45-48), 2010, 3005-3027.
[20] Ya, S., et al., An open-source ABAQUS implementation of the scaled boundary finite element method to study interfacial problems using polyhedral meshes, *Computer Methods in Applied Mechanics and Engineering*, 381, 2021, 113766.
[21] Greaves, D.M., Borthwick, A., Hierarchical tree-based finite element mesh generation, *International Journal for Numerical Methods in Engineering*, 45(4), 1999, 447-471.
[22] Liu, Y., et al., Automatic polyhedral mesh generation and scaled boundary finite element analysis of STL models, *Computer Methods in Applied Mechanics and Engineering*, 313, 2017, 106-132.
[23] Huang, Y., et al., 3D meso-scale fracture modelling and validation of concrete based on in-situ X-ray Computed Tomography images using damage plasticity model, *International Journal of Solids and Structures*, 67, 2015, 340-352.
[24] Zhang, J., Song, C., A polytree based coupling method for non-matching meshes in 3D, *Computer Methods in Applied Mechanics and Engineering*, 349, 2019, 743-773.
[25] Fix, G.J., *A Rational Finite Element Basis (Eugene L. Wachpress)*, Society for Industrial and Applied Mathematics, 1978.
[26] Nguyen-Xuan, H., et al., A polytree-based adaptive approach to limit analysis of cracked structures, *Computer Methods in Applied Mechanics and Engineering*, 313, 2017, 1006-1039.
[27] Persson, P.-O., Strang, G., A simple mesh generator in MATLAB, *SIAM Review*, 46(2), 2004, 329-345.
[28] Talischi, C., et al., PolyMesher: a general-purpose mesh generator for polygonal elements written in Matlab, *Structural and Multidisciplinary Optimization*, 45(3), 2012, 309-328.
[29] Talischi, C., et al., Polygonal finite elements for topology optimization: A unifying paradigm, *International Journal for Numerical Methods in Engineering*, 82(6), 2010, 671-698.
[30] Manual, A.S.U.S., Abaqus 6.11. http://130.149, 2012. 89(2080): p. v6.
[31] Liu, G., et al., A linearly conforming point interpolation method (LC-PIM) for 2D solid mechanics problems, *International Journal of Computational Methods*, 2(4), 2005, 645-665.
[32] Liu, G., et al., A linearly conforming radial point interpolation method for solid mechanics problems, *International Journal of Computational Methods*, 3(4), 2006, 401-428.
[33] Wolf, J.P., Song, C., *Finite-element modelling of unbounded media*, Wiley Chichester, 1996.
[34] Deeks, A.J., Wolf, J.P., A virtual work derivation of the scaled boundary finite-element method for elastostatics, *Computational Mechanics*, 28(6), 2002, 489-504.
[35] Song, C., A matrix function solution for the scaled boundary finite-element equation in statics, *Computer Methods in Applied Mechanics and Engineering*, 193(23-26), 2004, 2325-2356.

ORCID iD

Boonchai Phungpaingam https://orcid.org/0000-0002-5603-8345
Suthee Piyaphipat https://orcid.org/0000-0002-0945-7459
Kamtornkiat Musiket https://orcid.org/0000-0002-4794-5824

How to cite this article: Phungpaingam B., Piyaphipat S., Musiket K. Accuracy and Convergence Rate Comparative Investigation on Polytope Smoothed and Scaled Boundary Finite Element, *J. Appl. Comput. Mech.*, 9(1), 2023, 226–238. https://doi.org/10.22055/jacm.2022.41006.3689